ADVANCED FUNCTIONAL MATERIALS
www.afm-journal.de

Stretchable Anti-Fogging Tapes for Diverse Transparent Materials

Shaoting Lin, Yueying Yang, Jiahua Ni, Yoichiro Tsurimaki, Xinyue Liu, Baoyang Lu, Yaodong Tu, Jiawei Zhou, Xuanhe Zhao,* and Gang Chen**

Surface wetting prevents surface fogging on transparent materials by facilitating filmwise condensation with specific chemistry, but suffers from material and geometry selectivity. Extreme environments associated with high humidity and mechanical loading further limit their anti-fogging persistence. Here, a stretchable anti-fogging tape (SAT) that can be applied to diverse transparent materials with varied curvatures for persistent fogging prevention is reported. The SAT consists of three synergistically combined transparent layers: i) a stretchable and tough layer with large elastic recovery, ii) an endurant anti-fogging layer insensitive to ambient humidity, and iii) a robustly and reversibly adhesive layer. The SAT maintains high total transmittance (>90%) and low diffuse transmittance (<5%) in high-humidity environments, under various modes of mechanical deformations, and over a prolonged lifetime (193 days tested so far). Two applications are demonstrated, including the SAT-adhered eyeglasses and goggles for clear fog-free vision, and the SAT-adhered condensation cover for efficient solar-powered freshwater production.

1. Introduction

Transparent materials allowing light to pass them through without appreciable light scattering are indispensable for a wide range of applications[1,2] ranging from protective personnel equipment, optical instruments to solar-powered devices. When exposed to high-humidity environments or sudden change of temperature, surface fogging on transparent materials causes unintended light scattering,[3] followed by decreased visibility of optical devices,[4] lowered energy-conversion efficiency of solar stills[5] and solar cells,[6] and reduced crop yield in greenhouses.[7] Fogging on glasses also induces annoyance in daily life, and especially triggers health risks in fighting the COVID-19 pandemic as it increases the frequency of hand-face touching.[8]

Surface fogging is caused by droplet condensation on the surface which scatters light, and it can be avoided by facilitating filmwise condensation through surface wetting.[2,9–11] One way is to spray hydrophilic agents onto the surface,[11] but it suffers from a short lifespan (less than a few days) due to the weak interaction between the hydrophilic agents and the surface (Figure S1a, Supporting Information). Micro- and nano-fabrication are also used to engineer surface topology for modifying surface hydrophobicity,[12–14] but their manufacturing processes are technically complicated and time-consuming, thereby limited to laboratory research and impractical for large-scale massive production.[15] Whereas strong anchorage of cross-linked hydrogels to transparent materials has been developed to prevent surface fogging,[10] it usually leads to the reduced transparency in high-humidity environments due to the swelling-induced mechanical instabilities of hydrogels (Figure S1b, Supporting Information). Additionally, the above-mentioned anti-fogging methods are usually selective to a certain specific transparent material. For example, the method of covalently anchoring hydrophilic polysaccharides to glass[16] cannot be applied to polyethylene films due to the different interfacial chemistry. The challenges associated with existing anti-fogging methods are further amplified when transparent materials are curved (as in eyeglasses) and/or experience large deformations (as in stretch wraps). Thus, a universal strategy to maintain anti-fogging performance of transparent materials in humid and dynamic environments for a prolonged period of time remains a prevailing challenge.

Here, we propose a universal anti-fogging strategy based on a stretchable anti-fogging tape (SAT) that can be adhered to a wide range of transparent materials with various curvatures for persistent fogging prevention. The SAT synergistically integrates three distinct layers to address the above-mentioned limitations (**Figure 1**a): i) a stretchable intermediate layer with

Dr. S. Lin, Y. Yang, Dr. J. Ni, Y. Tsurimaki, X. Liu, Prof. B. Lu, Dr. Y. Tu, Dr. J. Zhou, Prof. X. Zhao, Prof. G. Chen
Department of Mechanical Engineering
Massachusetts Institute of Technology
Cambridge, MA 02139, USA
E-mail: shaoting@mit.edu; zhaox@mit.edu; gchen2@mit.edu
Dr. J. Zhou
Department of Materials Science and Engineering
Stanford University
Stanford, CA 94305, USA
Prof. X. Zhao
Department of Civil and Environmental Engineering
Massachusetts Institute of Technology
Cambridge, MA 02139, USA
The ORCID identification number(s) for the author(s) of this article can be found under https://doi.org/10.1002/adfm.202103551.

DOI: 10.1002/adfm.202103551

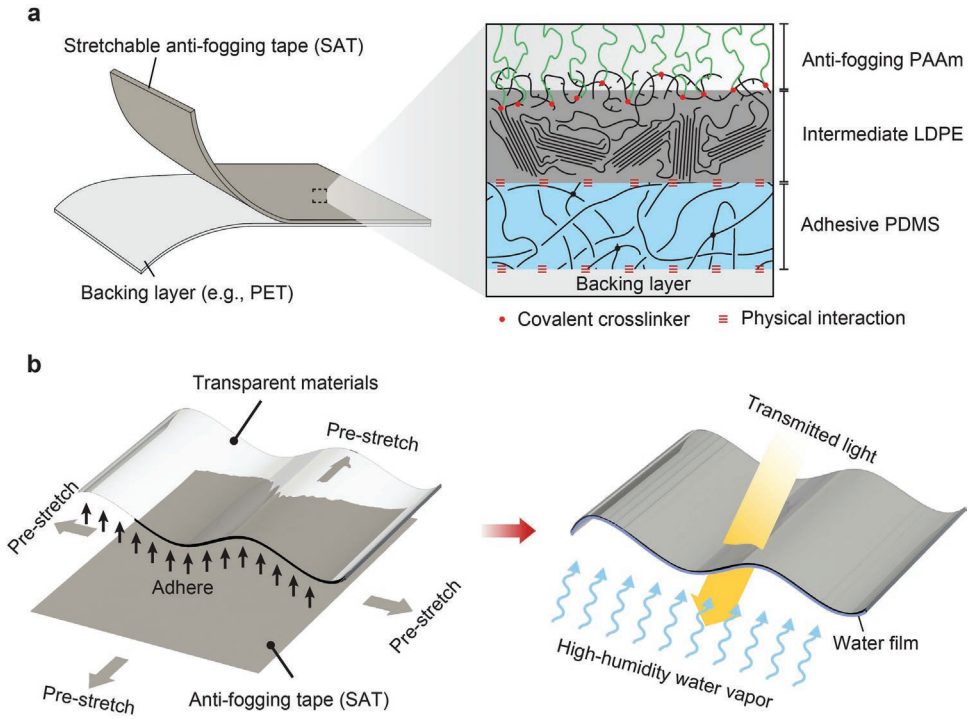

Figure 1. Schematic illustration of stretchable anti-fogging tape (SAT) applicable to diverse transparent materials with various curvatures. a) The SAT consists of three synergistically combined transparent layers: i) a stretchable middle layer with high elastic recovery made of low-density polyethylene (LDPE) to keep transparent materials tightly bound, ii) an anti-fogging top layer made of uncross-linked polyacrylamide (PAAm) to impart hydrophilicity to transparent materials, and iii) an adhesive bottom layer made of loosely cross-linked polydimethylsiloxane (PDMS) to form robust yet reversible adhesion between transparent materials and SATs. The SAT is originally adhered to a backing layer (e.g., PET) and can be readily peeled from the backing layer for usage. b) Schematic illustration of the working principle for applying the SAT. Once peeled from the backing layer, the SAT is first pre-stretched to remove wrinkles from its surface, and thereafter adhered to versatile transparent materials with various curvatures with seamless contact. When exposed to high-humidity environments, the transparent materials with SATs facilitate filmwise condensation, allowing the incident light to transmit them through with negligible light scattering.

high elastic recovery made of low-density polyethylene (LDPE) to keep the SAT tightly bound to transparent materials, ii) an anti-fogging top layer made of uncross-linked polyacrylamide (PAAm) to impart hydrophilicity to transparent materials, and iii) an adhesive bottom layer made of loosely cross-linked polydimethylsiloxane (PDMS) to form robust yet reversible adhesion between transparent materials and the SAT. Given these superior mechanical and physical properties, the SAT can be elastically pre-stretched and conformably adhered to targeted transparent substrates with seamless contact and no surface wrinkles, thereby effectively preserving the high transparency of the pristine transparent materials adhered with SAT (Figure 1b). We show that the SATs can be broadly applied to diverse transparent materials including glass, polyethylene (PE), polyethylene terephthalate (PET), polystyrene (PS), poly(methyl methacrylate) (PMMA), and PDMS. Meanwhile, the SATs can be conformably adhered to curved transparent surfaces with varied radii of curvature. The SAT can effectively maintain high total transmittance (>90%) and low diffuse transmittance (<5%) in high humidity environments. Such anti-fogging performances further persist during the 193-day testing period, even under various modes of mechanical loadings such as uniaxial tension, punching, and cyclic scratching. We further demonstrate that the SAT can be readily integrated with eyeglasses and protective goggles for clear fog-free vision and used as the condensation cover in a solar still to improve its efficiency of freshwater production.

2. Results and Discussion

2.1. Fabrication of Stretchable Anti-Fogging Tapes

To fabricate the stretchable anti-fogging tape, we biaxially pre-stretch an LDPE film and tightly attach and fix the pre-stretched LDPE film to a flat surface (e.g., acrylic substrate). The pre-stretch of the LDPE film can effectively eliminate its surface wrinkles, which otherwise reduces its optical transparency. On the upper surface of the prestretched LDPE film, we spin coat a layer of loosely cross-linked PDMS, followed by thermal curing at a mild temperature (i.e., 50 °C) for 2 h. We select a mild temperature for PDMS curing to prevent surface wrinkles induced by the thermal-induced deformation of the LDPE film. Once the PDMS layer is cured, we adopt the benzophenone-induced grafting photopolymerization[17,18] to covalently graft long-chain polymers of hydrophilic PAAm to the branched polymers of LDPE (Figure 1a). The surface with grafted PAAm chains of the resultant SAT film is thoroughly rinsed with deionized water to remove the unreacted reagents (i.e., acrylamide monomers) (Figure S2, Supporting Information). We

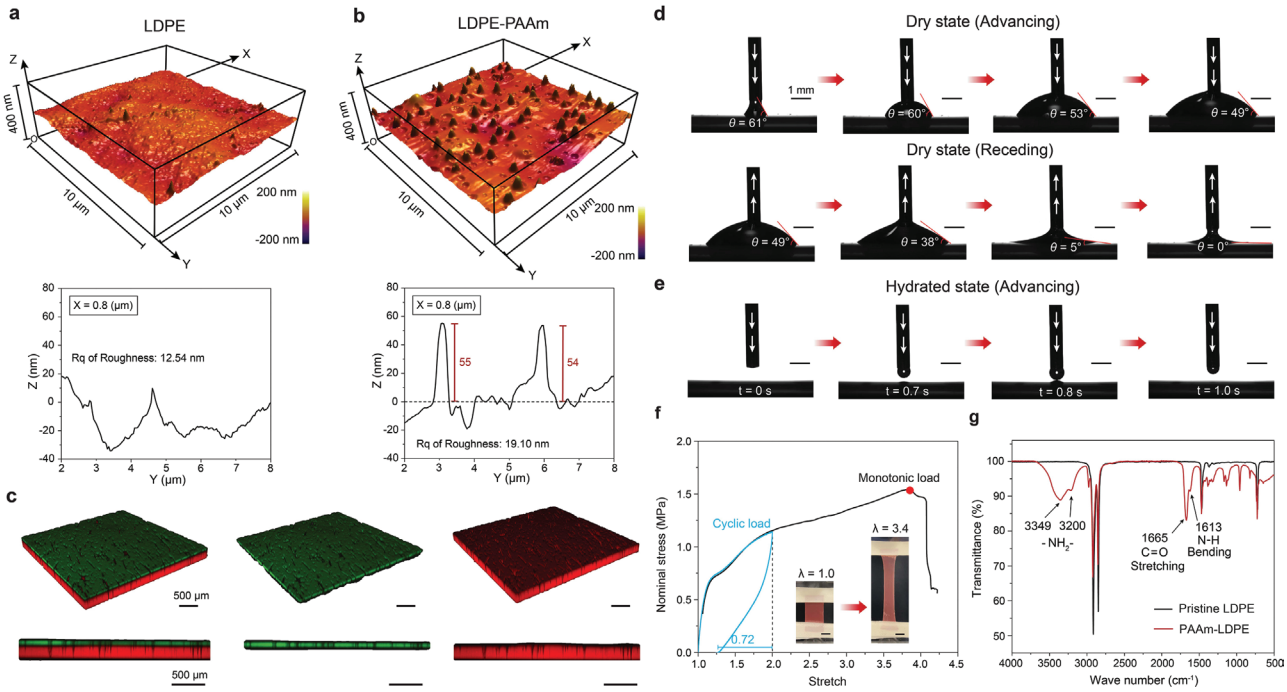

Figure 2. Surface and mechanical characterizations of the stretchable anti-fogging tape. a) AFM surface topology of the pristine LDPE film, measuring its root mean square of roughness. b) AFM surface topology of the LDPE-PAAm film, measuring the thickness of the PAAm layer and its root mean square of roughness. c) Confocal microscopy images of the anti-fogging tape to illustrate the uniform thickness of the PAAm layer in the hydrated state. PDMS and PAAm are stained with Nile red and fluorescein, respectively. d) Contact angle measurements of the anti-fogging tape in the dry state. e) Contact angle measurement of the anti-fogging tape in the hydrated state. f) Nominal stress versus stretch curves of SAT under monotonic uniaxial tensile loading and cyclic uniaxial tensile loading. The red dot indicates the failure point. Inset images showing the SAT at undeformed state (i.e., $\lambda = 1$) and deformed state (i.e., $\lambda = 3.4$). g) Transmission FTIR spectrum of the pristine LDPE film and the LDPE-PAAm film. The NH_2 at 3200 and 3349 cm^{-1}, the C=O stretching at 1665 cm^{-1}, and N-H bending at 1613 cm^{-1} indicate the anchored polyacrylamide chains. The scale bars in (c–f) are 500 μm, 1 mm, 1 mm, and 10 mm, respectively.

further perform the Fourier-transform infrared spectroscopy (FTIR) to characterize the chemical bonds of the SAT film after thorough rinsing with deionized water. As shown in **Figure 2**g, the resultant SAT film shows pronounced peaks associated with amide groups, indicating that the interaction between PAAm and LDPE should be strong covalent anchorage rather than weak deposition or absorption of PAAm chains. The details on fabrication and chemical synthesis of the SAT are provided in Experimental Section and Figure S3, Supporting Information.

2.2. Surface and Mechanical Characterizations of Stretchable Anti-Fogging Tapes

We first perform atomic force microscopy to characterize the surface topology of the PAAm layer in the dry state. As shown in Figure 2a,b, the thickness of the PAAm layer is about 55 nm in the dry state and its root mean square roughness is 19.10 nm, slightly higher than the roughness of the pristine LDPE film (i.e., 12.54 nm). We further use the confocal microscopy imaging to visualize the PAAm layer in the hydrated state. The PDMS layer and the PAAm layer are stained with Nile red and fluorescein, respectively. As shown in Figure 2c, the thickness of the PAAm layer in the hydrated state is much greater than its thickness in the dry state due to the superior swelling of the grafted PAAm polymers.

We further conduct contact angle measurements to characterize the surface wetting property of the anti-fogging tape. As shown in Figure 2d and Video S1, Supporting Information, a total volume of 10 μL deionized water is deposited on the dry surface of the PAAm layer. As the volume of the deposited water increases, the advancing contact angle gradually decreases and reaches a steady-state value of 49°. As the volume of the deposited water decreases, the measured receding contact angle decreases drastically from 49° to 0°, suggesting the super hydrophilicity of the PAAm layer in the hydrated state. We further deposit deionized water on the hydrated surface of the PAAm layer (Figure 2e and Video S2, Supporting Information). The water droplet on the nozzle spreads out in 0.1 s once it contacts the PAAm layer, further demonstrating its super hydrophilicity.

In addition to surface characterizations, we also characterize mechanical properties of the SAT film. As shown in Figure 2f and Video S3, Supporting Information, the SAT can be stretched up to 3.8 times its original length without interfacial delamination. In addition, the SAT exhibits a remarkable elastic recovery with an elastic recoverable strain of 0.72 (Figure 2f), which keeps it tightly bound to targeted transparent materials. The elastic recoverable strain of the SAT exceeds that of the common transparent materials (e.g., <0.05 for PET, PS, PMMA).[19] The SAT is also tough with a high fracture energy of 2126 J m^{-2} (Figure S4 and Video S4, Supporting Information), which renders its

mechanical robustness when elastically pre-stretched and conformably adhered to targeted transparent materials. In addition, we characterize the adhesiveness between the SAT and the backing layer (i.e., PET), which demonstrates a robust and reversible adhesive strength of 4 kPa for 1000 cycles of attachment and detachment (Figure S5, Supporting Information).

2.3. Optical Characterizations of Stretchable Anti-Fogging Tapes

We first characterize water condensation on both the pristine LDPE film and the LDPE-PAAm film. As shown in Figure S6a, Supporting Information, a water container is heated by a hot plate at a controlled temperature for 20 min to reach the steady state. A thermocouple is used to monitor the temperature of the water inside the container. Thereafter, the sample is covered on top of the water container with heated water vapor condensing on its bottom surface. We use optical microscopy to capture the real-time morphology of the condensed water. As shown in Figure S6b,c, Supporting Information, the pristine LDPE film facilitates dropwise condensation due to its hydrophobicity, while the LDPE-PAAm film promotes filmwise condensation because of its super hydrophilicity in the hydrated state.

To systematically characterize the effect of the condensed water on optical properties of the film, we further perform UV–vis–NIR spectroscopy to quantify the total transmittance and diffuse transmittance throughout samples before and after condensation (Video S5, Supporting Information). The measurements follow the standard of ASTM D1003. The total transmittance characterizes the total percentage of the incident light directly and diffusely transmitting through the sample, while the diffuse transmittance measures the percentage of the incident light diffusely transmitting through the sample. As illustrated in **Figure 3**a,b, the total transmittance T_t is calculated by the ratio of the light transmitted through the specimen T_2 versus the incident light T_1, that is, $T_t = T_2/T_1$ (Figure 3a). The diffuse transmittance T_d is calculated by $T_d = [T_4 - T_3(T_2/T_1)]/T_1$, where T_3 is the light scattered by the instrument and T_4 is the light scattered by both the instrument and the sample (Figure 3b). When exposed to heated water vapor at 50 °C (the temperature refers to the measured temperature of the liquid water in the container), the total transmittance of the pristine LDPE decreases significantly from 92% to 75% in the visible spectrum and decreases from 92% to 60% in the near-infrared spectrum due to the backscattering of light by water droplets (Figure 3c,d). In contrast, the LDPE film with covalently grafted uncross-linked PAAm (i.e., LDPE-PAAm) shows negligible loss of transmittance over the entire spectrum in spite of a slight decrease of total transmittance between 1700 and 1800 nm due to the light absorption by water (Figure 3f,g). We also measure the diffuse transmittance of both the pristine LDPE and LDPE-PAAm to characterize their haze when exposed to heated water vapor at 50 °C. The diffuse transmittance of the pristine LDPE film increases from 8% to 48% in the visible spectrum due to its dropwise condensation (Figure 3e). In contrast, the filmwise condensation maintains a low diffuse transmittance of the LDPE-PAAm below 5% across the spectrum, manifesting the low haze of a uniform water film (Figure 3h). The total transmittance and diffuse transmittance of the LDPE-PAAm after condensation in this work outperform those of the commercially available anti-fogging products including the anti-fog spray (Optix55), anti-fog wipes (KarisVisual), anti-fog mirror window film (Kerkoor), and anti-fog greenhouse film (Agfabric) as summarized in Figure S7, Supporting Information. These commercially available anti-fogging products mostly rely on spraying hydrophilic agents or addition of surfactants.

Water vapor temperature is a well-known factor affecting the optical transparency of the film after condensation due to the altered size of the condensed water droplets.[20] As shown in Figure S8a, Supporting Information, the increase of the water vapor temperature drastically decreases the total transmittance of the pristine LDPE film because of the enlarged water droplet on the film. In contrast, the water vapor temperature has little effect on the LDPE-PAAm film (Figure S8b, Supporting Information), which indicates the water vapor temperature does not change the thickness of the condensed water film. We also check the effect of the coated PDMS layer on the optical properties of the SAT. As shown in Figure S9, Supporting Information, the PDMS layer slightly decreases the total transmittance from 92% to 88% in the visible and near-infrared spectrum and slightly increases the diffuse transmittance from 2% to 5% across the entire spectrum. In particular, we find the presence of the PDMS layer dramatically decreases the total transmittance in the ultraviolet spectrum because of the high absorption of ultraviolet light of PDMS.

To support the crucial role of filmwise water condensation in the high total transmittance of the LDPE-PAAm film, we then perform wave optics simulation based on the transfer matrix method for a two-layer structure made of a water film on top of a 20 μm-thick LDPE film. The predicted total transmittance for the 16-μm thick water film agrees well with the experimental measurement as shown in Figure 3g. We further carry out ray optics simulation in a pristine LDPE film with water droplets. By assuming the uniform droplet radius of 40 μm, the contact angle of 110° and the droplets area density of 0.55 as measured experimentally (Figure S6d, Supporting Information), the model predicts a drastic reduction of total transmittance, matching with the experimental data shown in Figure 3d. The details of the wave and ray optics modeling can be found in Experimental Section.

2.4. Persistence and Universality of Anti-Fogging Properties

Persistent anti-fogging properties is a central challenge faced by existing anti-fogging approaches but highly desirable for practical deployment.[21,22] Here, we show our approach can potentially address this challenge. As one example shown in Figure S1a, Supporting Information, the LDPE film sprayed with hydrophilic agents exhibits decreased optical transparency when the film is exposed to heated water vapor at 60 °C for 14 min (**Figure 4**a,c). The hydrophilic agents are washed away by condensed water on the surfaces continuously due to the weak interaction between hydrophilic agents and transparent materials.[2] As another example shown in Figure S1b, Supporting Information, the LDPE film covalently coated with a layer of cross-linked hydrogel loses its optical transparency when the film is exposed to heated water vapor at 60 °C for 20 min, because the cross-linked hydrogel tends to

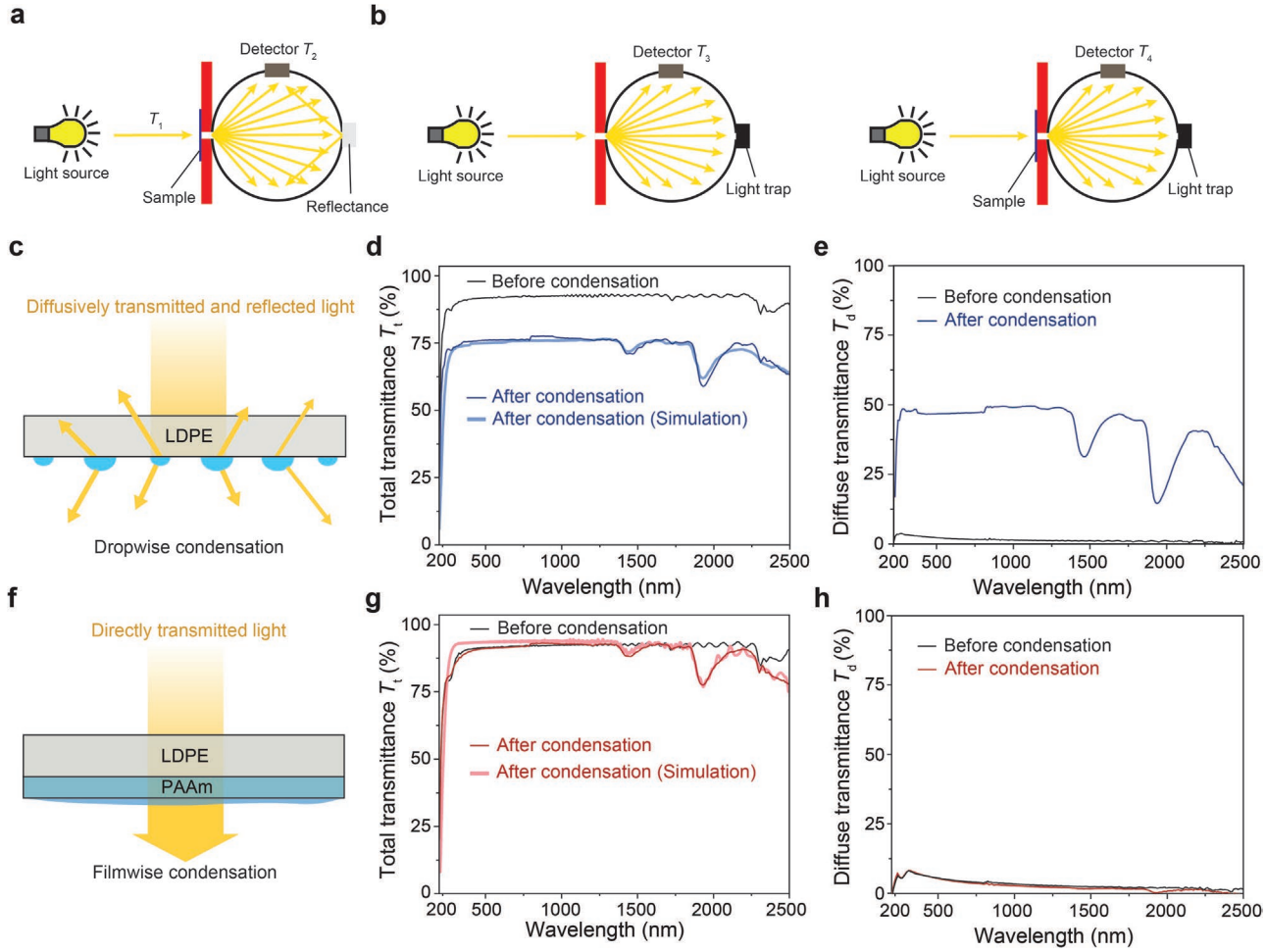

Figure 3. UV–vis–NIR characterization. a) Schematic illustration of the measurement of total transmittance $T_t = T_2/T_1$, where T_1 is the intensity of incident light and T_2 is the intensity of transmitted light in total. b) Schematic illustration of the measurement of diffuse transmittance $T_d = [T_4 - T_3(T_2/T_1)]/T_1$, where T_3 is the intensity of the scattered light by the instrument measured with no sample in position but with the light trap in position, and T_4 is the intensity of the diffusively transmitted light with both the sample and the light trap in position. c) Schematic illustration of the diffusively transmitted and reflected light in the pristine LDPE film. d) The measured total transmittance of the pristine LDPE film before condensation and after condensation when exposed to hot water vapor. The bold line is the corresponding simulation result of the total transmittance of the pristine LDPE film after condensation when exposed to hot water vapor. e) The measured diffuse transmittance of the pristine LDPE film before condensation and after condensation when exposed to hot water vapor. f) Schematic illustration of the directly transmitted light in the LDPE-PAAm film. g) The measured total transmittance of the LDPE-PAAm film before condensation and after condensation when exposed to hot water vapor. The bold line is the corresponding simulation result of the total transmittance of the LDPE-PAAm film after condensation when exposed to hot water vapor. h) The measured diffuse transmittance of the LDPE-PAAm film before condensation and after condensation when exposed to hot water vapor.

develop swelling-induced crease instability on the surface[23] (Figure 4b,c; Figure S1b, Supporting Information). In contrast, we show that both the covalent anchorage and uncrosslinked hydrophilic polymers in our approach are essential for long-term robust and humidity-insensitive optical properties (Figure 4a,b). The total transmittance of our LDPE-PAAm film can consistently maintain high total transmittance over 90% and low diffuse transmittance below 10% across the visible and near-infrared spectrum for 193 days (Figure 4c,d; Figure S10a,b, Supporting Information). The durable anti-fogging properties of our approach further justify that the interaction between PAAm and LDPE is strong covalent anchorage rather than weak deposition or absorption of PAAm polymers.

We further testify the anti-fogging properties of the LDPE-PAAm film under various modes of mechanical loadings, including biaxial tension and dynamic scratching. We first apply punching loading on a circle-shaped film with a diameter of 65 mm to simulate the biaxial tensile loading. As shown in Figure 4e, the LDPE-PAAm film can maintain high total transmittance over 90% and low diffusive transmittance below 5% even when the punching displacement increases up to 15 mm. When the applied punching displacement reaches 20 mm, the diffuse transmittance increases due to the excessive plastic deformation induced in the film. Dynamic scratching is another common mechanical load that might damage the anchored PAAm layer. To simulate the load of dynamic scratching, we use a probe to compress the LDPE-PAAm film and apply a reciprocating motion of the probe. The compressive forces are monitored from 0 to 4.8 N, corresponding to the normal pressure of 0 to 20 kPa as the contact area between the probe

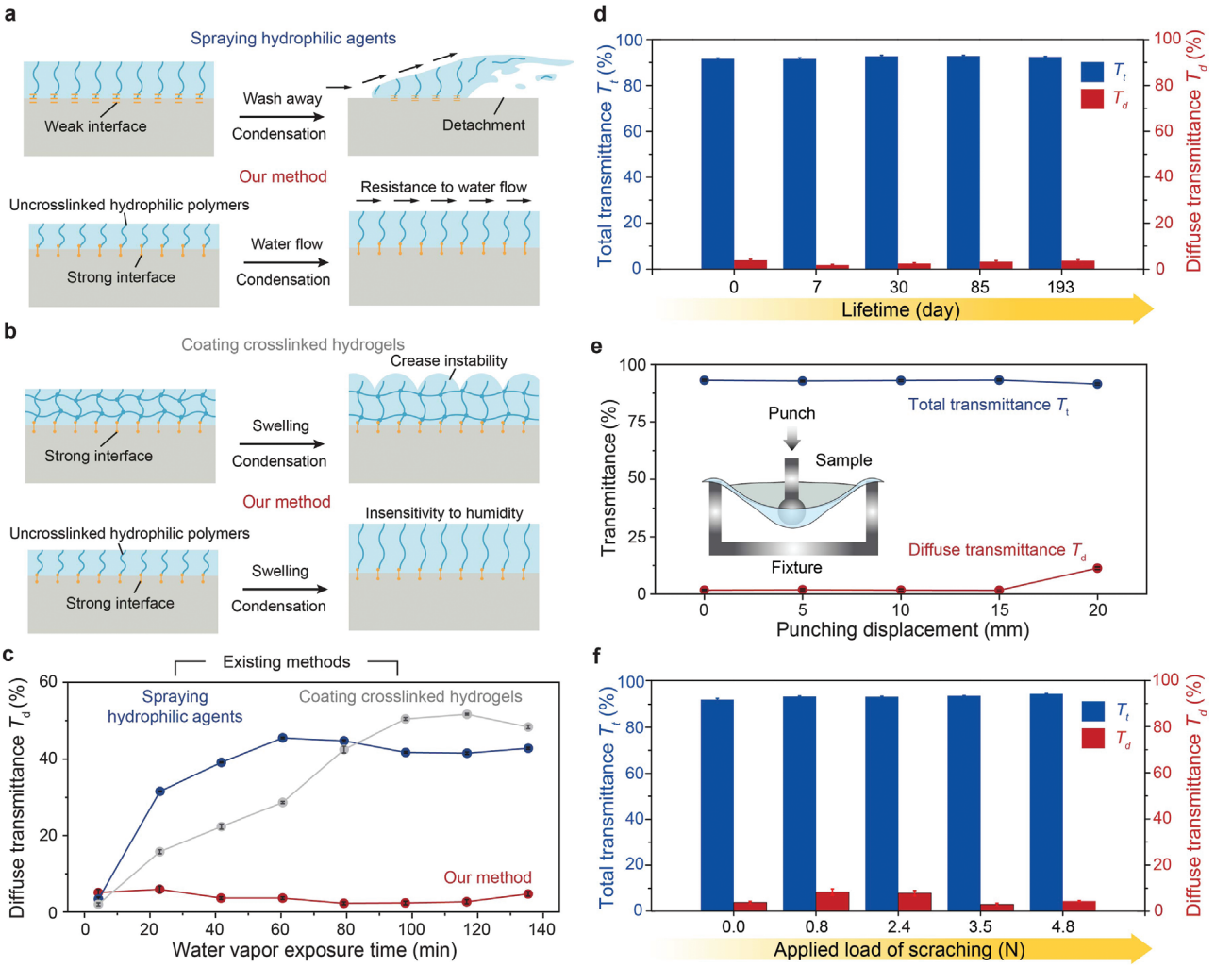

Figure 4. Characterizations of anti-fogging properties of the SAT in extreme environments. a) The existing method of spraying hydrophilic agents suffers short lifetime due to the weak interface between the hydrophilic agents and transparent materials. In contrast, our method of covalently grafting uncross-linked hydrophilic polymers maintains the mechanical robustness by resisting condensed water flow. b) The existing method of coating cross-linked hydrogels suffers low optical transparency when exposed to high-humidity environments because the swelling of cross-linked hydrogels results in crease instability. In contrast, swelling of uncross-linked hydrophilic polymers in our method does not affect the transparency of the film, giving high transparency in high-humidity environments. c) Comparison of the measured diffuse transmittance among existing anti-fogging methods and our method as a function of water vapor exposure time. d) Measured total transmittance and diffuse transmittance of the LDPE-PAAm film through the test period over 193 days. e) Measured total transmittance and diffuse transmittance of the LDPE-PAAm film at various punching displacements of 0, 5, 10, 15, and 20 mm. f) Measured total transmittance and diffuse transmittance of the LDPE-PAAm film at various loads of dynamic scratching.

and the LDPE-PAAm film is around 200 mm^2. Both the total transmittance and diffuse transmittance are measured after 100 cycles of dynamic scratching under various compressive forces. As shown in Figure 4f and Figure S10c,d, Supporting Information, the LDPE-PAAm maintains a high total transmittance above 90% and low diffuse transmittance below 10%, indicating its remarkable mechanical robustness under various loads of dynamic scratching.

To demonstrate the anti-fogging tape can be applicable to universal substrates, we adhere the SAT to substrates with diverse materials (e.g., PET, PDMS, PMMA, PS, glass) and geometries (e.g., cylindrical tubes with varied curvatures). Given the high stretchability, large elastic recovery, high toughness, and reversible adhesion of SAT, the SAT can be pre-stretched and then adhered to substrates with seamless contact and no surface wrinkles. When further exposed to heated water vapor, the taped transparent materials show superior anti-fogging properties, giving clear fog-free vision (**Figure 5**a; Videos S6–S9, Supporting Information). The total transmittance of the visor materials with SATs can reach as high as 90%, and the diffuse transmittance is as low as about 5% in the visible spectrum (Figure 5b; Figure S11, Supporting Information). We further conformably attached the SAT to the inner surfaces of PMMA tubes with altered radii of curvature ranging from 3.2 to 19.1 mm. As shown in Figure 5c, the SAT can effectively impart the curved surfaces with anti-fogging properties (high total transmittances and low diffuse transmittances), giving clear fog-free vision when exposed to high humidity and

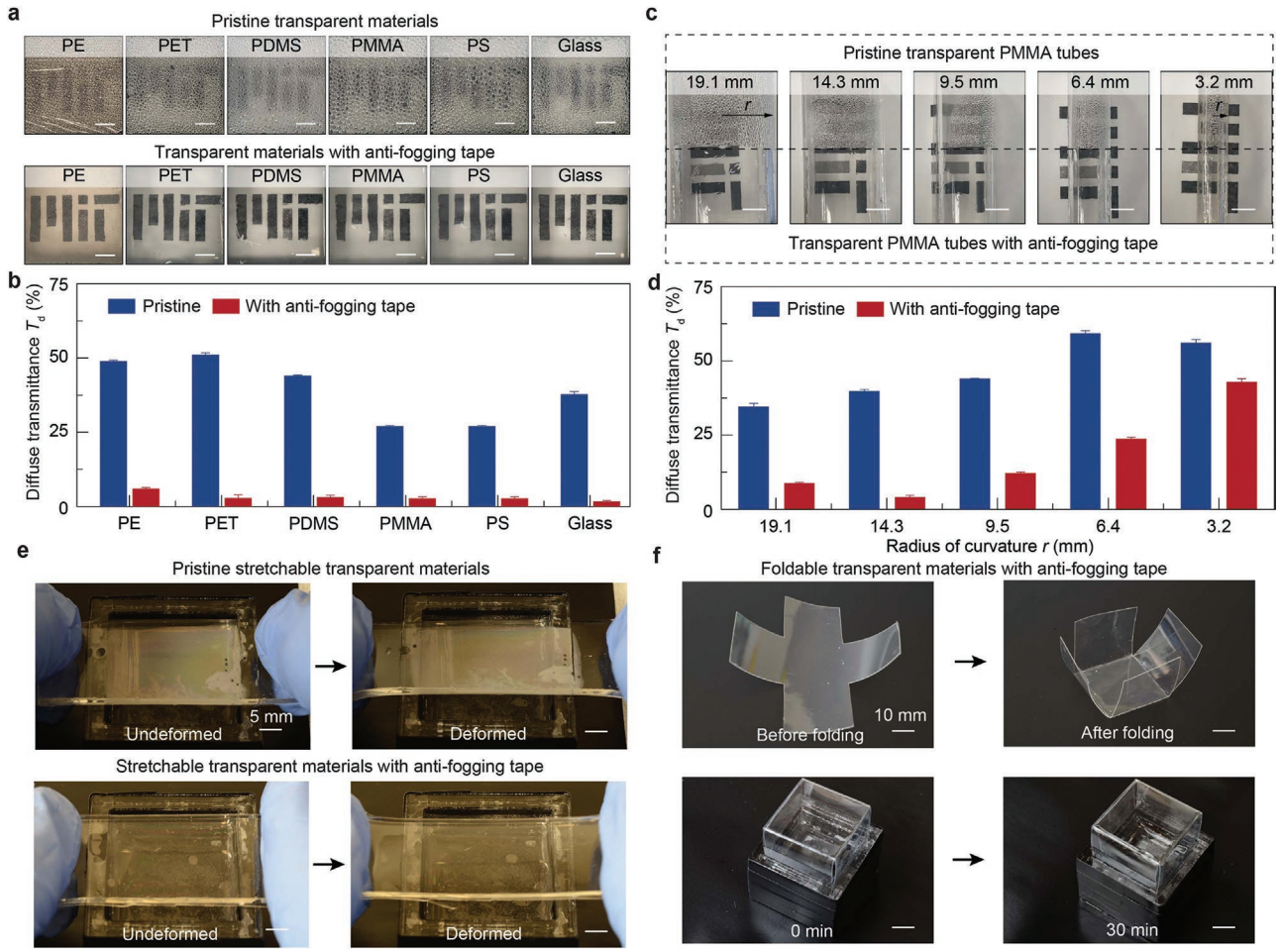

Figure 5. Anti-fogging properties for diverse transparent materials. a) Dropwise condensations on the pristine transparent films (i.e., PE, PET, PDMS, PMMA, PS, Glass) block the visions when exposed to heated water vapor due to their fogging surfaces. Filmwise condensations on the same films with anti-fogging tape maintain clear visions when exposed to heated water vapor due to their anti-fogging surfaces. b) Measured diffuse transmittance of the pristine transparent films (i.e., PE, PET, PDMS, PMMA, PS, Glass) and the same films with anti-fogging tape. c) Dropwise condensations on the pristine curved PMMA tubes with various radii of curvature (i.e., 3.2, 6.4, 9.5, 14.3, 19.1 mm) block the visions when exposed to heated water vapor due to their fogging surfaces. Filmwise condensations on the same tubes with anti-fogging tape maintain clear visions when exposed to heated water vapor due to their anti-fogging surfaces. d) Measured diffuse transmittance of the pristine curved PMMA tubes with various radii of curvature (i.e., 3.2, 6.4, 9.5, 14.3, 19.1 mm) and the same tubes with anti-fogging tape. e) Demonstration of fogging on the pristine stretchable transparent material and anti-fogging on the stretchable transparent material with anti-fogging tape. f) Demonstration of anti-fogging on the foldable transparent material with anti-fogging tape. The scale bars in (a), (c), (e), (f) are 10, 5, 5, and 10 mm.

high temperature (Figure 5d; Video S10, Supporting Information). Given the high stretchability of the anti-fogging tape, we further demonstrate new functions for eliminating fog on soft, stretchable, and foldable transparent materials. As shown in Figure 5e, we demonstrate the stretchable transparent materials (i.e., PDMS) with anti-fogging tape can combat fogging issue at a highly deformed state when exposed to heated water vapor (60 °C). As another example shown in Figure 5f, we further show a foldable transparent material can maintain its transparency for 30 min when exposed to heated water vapor (60 °C).

2.5. Applications of Stretchable Anti-Fogging Tapes

After validation of the superior anti-fogging performance and remarkable mechanical robustness of the SAT, we further explore the applications of SATs on optical and solar devices that are susceptible to fogging, including eyeglasses, goggles, and solar stills.

First, we apply our SAT to solve the fogging issue of eyeglasses and safety goggles (**Figure 6**a). As shown in Figure 6b,c the lens with SAT attached at the inner surface can maintain clear vision when exposed to humid environment and a sudden change of temperature. To test the performance in real environments, we wear the glasses with a SAT adhered on the left lens. As shown in Figure 6d–f, our SAT can effectively maintain the clear vision in the indoor environment with a room temperature of 22 °C and at the outdoor environment with a cold temperature of −5 °C. In comparison, the fogging on the pristine lens severely blocks the vision.

Next, we demonstrate the use of LDPE-PAAm film as a condensation cover in a sunlight-powered water purification

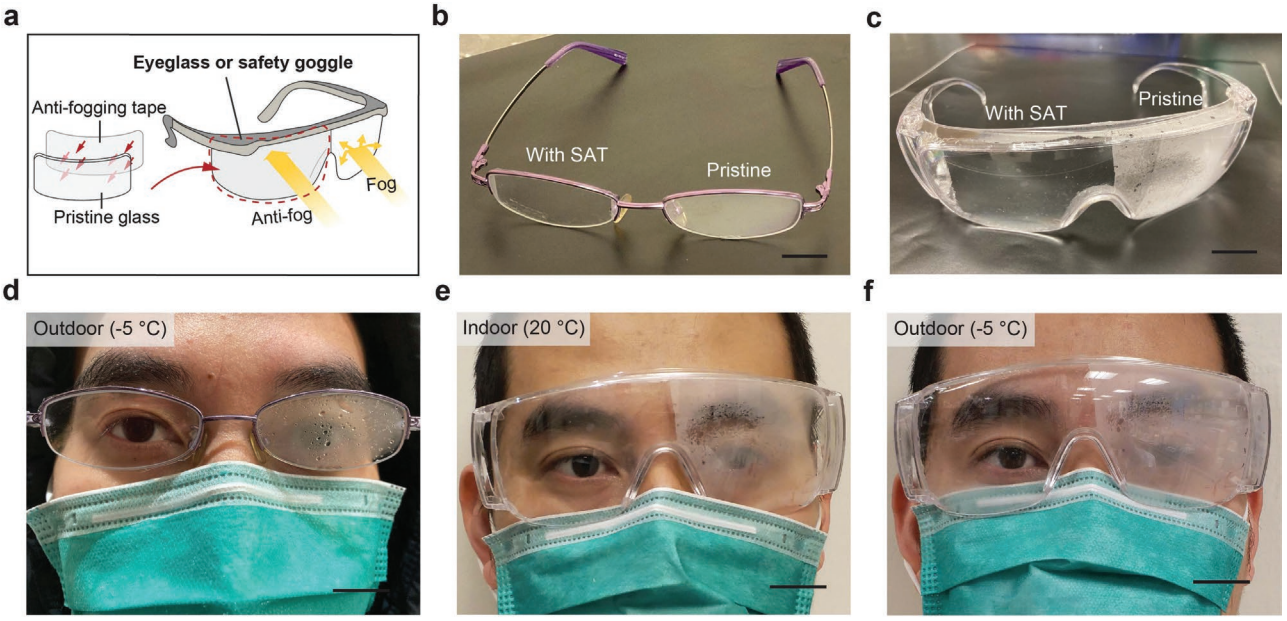

Figure 6. Anti-fogging eyeglasses and protective goggles. a) Schematic illustration of the working principle for applying the stretchable anti-fogging tape to eyeglasses and safety goggles. b) The resultant eyeglass with anti-fogging tape adhered onto the inner surface of the right-side glass. c) The resultant goggle with anti-fogging tape adhered onto the inner surface of the left-side goggle. d) Outdoor fogging test of eyeglass at the temperature of −5 °C. e) Indoor fogging test of protective goggle at room temperature of 20 °C. f) Outdoor fogging test of protective goggle at the temperature of −5 °C. The scale bars in (b–f) are 20 mm.

system to illustrate its potential for efficient solar energy harvesting and water desalination (**Figure 7**a). Normally, the evaporated water vapor from brine can condense as droplets on the collection cover of the solar still, resulting in a reduction of optical transparency by ≈35%.[5] We build a prototype of the water purification system under natural sunlight, which consists of a black super-absorbent foam as the absorber, the LDPE-PAAm film as the condensation cover, a beaker as the purified water collector, and a bubble wrap as the thermal insulation layer (Figure S12, Supporting Information). A metallic ball is placed on top of the condensation cover, directing the condensed water to drip into the beaker by gravity. As a control comparison, we also set up a reference system with the pristine LDPE film as the condensation cover.

We conduct outdoor water purification tests at Massachusetts Institute of Technology campus from 8:00 to 20:00 on June 23, 2020. Figure S13a, Supporting Information, plots the recorded solar flux with a total solar energy of 7.17 kW·h m^{-2} during the testing period. Figure S13b,c, Supporting Information, shows the measured ambient temperature and relative humidity on the same day with an average value of 35 °C and 40%, respectively. Purified water is collected around every hour. The LDPE-PAAm film as the condensation cover maintains high transparency with negligible fogging for the entire sunny day, while the pristine LDPE film shows significant surface fogging from 9:00 (Figure 7b). Due to the superior anti-fogging performance, the LDPE-PAAm film enables the solar water purification system to reach a water collection rate of 3.8 L m^{-2} per day, 2.4 times that of the reference system (pristine LDPE film as the condensation cover, 1.6 L m^{-2} per day) (Figure 7c). The reduction of the light backscattering by the LDPE-PAAm condensation cover is further validated by the increased absorber temperature, vapor temperature, and bulk water temperature shown in Figure S14, Supporting Information. To test the durability of the film after long-term storage, we perform the other outdoor water purification test from 8:00 to 20:00 on Sep 8, 2020. Our water purification system with the HPE film as the condensation cover still shows a 190% boost for freshwater production as shown in Figure 7d. The weather conditions on Sep 8, 2020, are summarized in Figure S13d,e, Supporting Information. To further demonstrate the capability of solar-powered water purification, we measure the concentrations of four primary ions (Na^+, Mg^{2+}, K^+, and Ca^{2+}) before and after desalination as shown in Figure 7e. These ions in the collected water are significantly reduced and below the values for drinkable water according to US Environmental Protection Agency (EPA).[24]

We further evaluate the collection efficiency of both of the water purification systems, using the following definition:[25]

$$\eta_{\text{water}} = \frac{m_{\text{water}} h_{\text{water}} + m_{\text{water}} C_p \left(T_{\text{water}} - T_{\text{ambient}}\right)}{A_{evap} \int q_{solar} dt} \quad (1)$$

where m_{water} is the collected purified water per day, h_{water} = 2400 kJ kg^{-1} is the latent heat for evaporation of water at 50 °C, C_p = 4186 J/(°C kg) is the specific heat of water, T_{water} is the temperature of water at the surface with an average value of 50 °C for the HPE film and 45 °C for the pristine PE film, T_{ambient} is the ambient temperature with an average value of 35 °C, A_{evap} is the evaporation area, and q_{solar} is the time-dependent solar flux. Following Equation (1), the water purification system using the LDPE-PAAm film as the condensation cover reaches a water collection efficiency as high as 36.2%, 2.4 times of the same system using the pristine LDPE film as the condensation cover (i.e., 15.1%). Note that the water collection efficiency for the

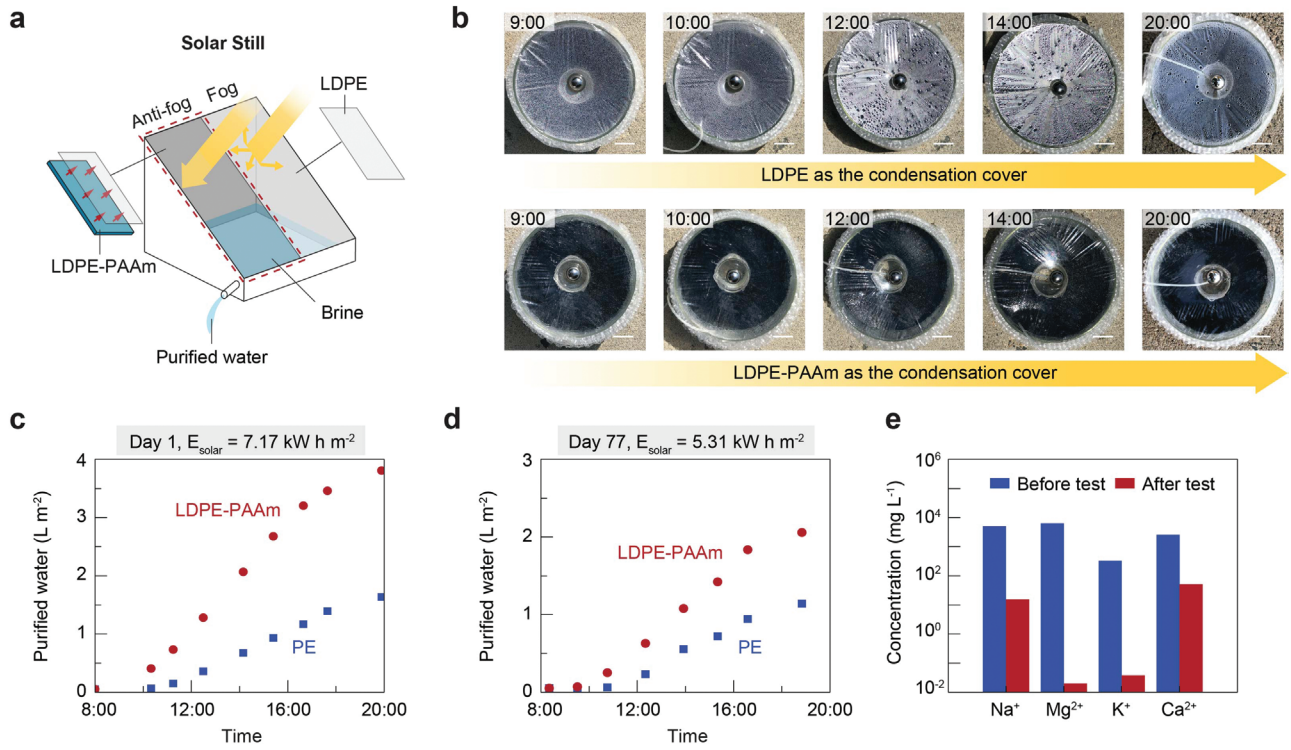

Figure 7. Outdoor water purification tests under natural sunlight. a) Schematic illustration of the design of solar still using LDPE-PAAm as the condensation cover to enhance solar-powered freshwater production. b) Images of two solar stills with the pristine LDPE film and the LDPE-PAAm film as the condensation cover from 09:00 to 20:00 on June 23, 2020. c) The collected purified water over time for the two water purification systems with the pristine PE film and LDPE-PAAm film as the condensation cover from 8:00 to 20:00 on June 23, 2020. d) The collected purified water over time for the two water purification systems with the pristine LDPE film and LDPE-PAAm film as the condensation cover from 8:00 to 20:00 on Sep 8, 2020 after prolonged storage of the film for 77 days. e) Measured concentration of the primary ions Na^+, Mg^{2+}, K^+, and Ca^{2+} before and after solar-powered desalination. The scale bars in (b) are 2.5 cm.

state-of-the-art floating solar still is 24%.[5] Our LDPE-PAAm film, as the simplest design of condensation structure, can be readily integrated with existing evaporation structures with no significant investment in cost while increasing the water collection efficiency.

3. Conclusions

Motivated by the ubiquitous fogging and their threatening effects on environment and human health, we report a universal anti-fogging approach by designing a stretchable anti-fogging tape (SAT) that can be generally applicable to diverse transparent materials and various curved surfaces of optical devices and solar products. We demonstrate the superior anti-fogging properties of the SAT with high total transmittance above 90% and low diffuse transmittance below 5% in high-humidity environments, under various modes of mechanical deformations (uniaxial tension, punching, and cyclic mopping), and over a prolonged lifetime (over 193 days tested so far). We show potential applications of the SAT for efficient solar stills and personal protective equipment. This work also suggests new applications of hydrogels towards functional flexible transparent materials by harnessing tailored properties of polyethylene films[6,26,27] and hydrogels.[28,29]

4. Experimental Section

Materials: Chemicals including acrylamide, benzophenone, Irgacure-2959, and Sylgard 184 were purchased from Sigma-Aldrich. Saran Premium Wrap as low-density polyethylene was purchased from Johnson. NHS-Fluorescein was purchased from Thermo Fisher Scientific. Visor materials including PET, Glass, PMMA were purchased from McMaster-Carr. All chemicals were used without further purification. Deionized water (from a Milli-Qsystem) was used throughout the experiments.

Fabrication of LDPE-PAAm: Figure S3, Supporting Information, schematically illustrates the procedure and benzophenone-induced grafting photopolymerization[17] for fabricating the LDPE-PAAm. The pristine low-density polyethylene film (Saran Premium Wrap) was first thoroughly cleaned with ethanol and deionized water, and completely dried with nitrogen gas. Thereafter, the benzophenone solution (10 wt% in ethanol) was applied onto the polyethylene film to evenly cover the entire surface for 10 min at room temperature. The benzophenone-treated polyethylene film was washed with ethanol three times and completely dried with nitrogen gas. Precursor solution of hydrogel polymers was prepared by mixing aqueous solutions of hydrophilic monomer (i.e., acrylamide) and hydrophilic initiator (i.e., Irgacure-2959, 1 wt%). The typical concentration of the hydrophilic monomer ranges from 5 to 40 wt%, which determines the chain density anchored on the surfaces of polyethylene film. The mixture of the precursor solution was poured onto the benzophenone-treated polyethylene film in an acrylic mold and then covered by a glass plate with a hydrophobic coating. Both the precursor solution and the benzophenone-treated polyethylene film were subjected to ultraviolet irradiation in an ultraviolet chamber (365 nm ultraviolet; UVP CL-1000) for an hour. Under UV radiation,

the hydrophilic monomer forms PAAm polymers via free radical polymerization. Meanwhile, surface absorbed benzophenone mediates the grafting of PAAm polymers onto the reactive sites on the polyethylene chains. After UV radiation, the treated polyethylene film was thoroughly rinsed with deionized water to remove the unreacted reagents on the surface of the LDPE film.

Fabrication of SAT: A pristine LDPE film was first pre-stretched and tightly attached to an acrylate plate with no surface wrinkles. Thereafter, the pre-stretched LDPE film was uniformly coated with a PDMS solution, using the spin coater (Specialty coating systems, 6800 Spin Coater Series) with a rotation speed of 250 rpm for 3 min. The thickness of the PDMS layer can be tuned by adjusting the rotational speed. The mixing ratio of PDMS is set as 1/30 for the reversible adhesion. The entire sample was further cured at a mild temperature (i.e., 50 °C) for 12 hours to ensure no surface wrinkles formed by the thermal-induced deformation of the LDPE film. Once the PDMS layer is cured, we followed the same protocol of synthesizing LDPE-PAAm to covalently graft uncrosslinked PAAm on the other surface of the LDPE film. The resultant SAT consists of a laminated structure with the LDPE film as the intermediate layer, the PDMS as the adhesive layer, and the PAAm as the anti-fogging layer.

AFM Imaging: AFM topology images were acquired with an atomic force microscope (MFP-3D, Asylum Research). Dry freestanding pristine LDPE and SAT films were directly attached onto the sample stage with a double-sided carbon tape. Surface topology was evaluated for areas covering $10 \times 10\ \mu m^2$.

Confocal Microscopy Imaging: Due to the optical transparency of the SAT film, different dyes were utilized to facilitate imaging and characterization of the SAT film. A hydrophobic Nile red dye ($\lambda_{emission} \approx$ 600 nm) was added to Sylgard 184 mixture to allow the visualization of the PDMS layer while the anti-fogging tape was immersed in an aqueous NHS-fluorescein solution ($\lambda_{emission} \approx 518$ nm) to enable the visualization of the PAAm layer.

Contact Angle Measurement: A total volume of 10 µL deionized water was deposited on both dry and hydrated surfaces of the pristine LDPE film and the PAAm layer of the anti-fogging tape. Videos were recorded to measure the advancing and receding contact angles.

UV–Vis–NIR Measurement: The UV–vis–NIR measurement was conducted by the Cary 5000 UV–vis–NIR spectrophotometer (Agilent Technologies), following the standard ASTM D1003. The first test was run with no specimen in position but with a standard high-reflectance reference material in position to measure the intensity of incident light T_1. The second test was run with both the specimen and the reference in position to measure the total light transmitted through the specimen T_2. The total transmittance can be calculated by the ratio of T_2 over T_1 (e.g., $T_t = T_2/T_1$). The third test was run with no specimen in position but with a light trap in position to measure the light scattered by the instrument T_3. The last test was run with both specimen and light trap in position to measure the light scattered by the instrument and the specimen T_4. The diffuse transmittance can be calculated by $T_d = [T_4 - T_3(T_2/T_1)]/T_1$.

Simulation of the Total Transmittance of the Films after Condensation: The wave optics simulation of a LDPE-PAAm was performed by the transfer matrix method. The structure is shown in Figure S6, Supporting Information, where it is a two-layer structure made of the LDPE film on top of a water film. The entire structure is in the air. The incident light is normally incident on the structure from the LDPE film side and is assumed unpolarized because the primary interest is in solar radiation as well as ambient light. The optical properties of water were taken from the work.[30] The optical properties of LDPE reported in the literature [31] were used for wavelengths from 1.1 to 2.5 µm and the complex refractive index at the shortest wavelength reported in the literature,[31] that is, $\lambda = 1.1$ µm, was extrapolated to the shorter wavelengths. To take into account the exponential increase of the absorption coefficient of LDPE in the UV range, their optical properties at the UV range ($\lambda \leq 0.17$ µm) reported in the literature[32] was approximated as $k = 8.54 \times 10^{-10}$ exp $(1.55 \times 10^{-15}\ \omega)$ and was smoothly connected to those at the visible range. As a result, the optical properties of LDPE used in the simulation are shown in Figure S16a, Supporting Information. The thickness of the LDPE film was determined as 20 µm by fitting the predicted total transmittance to the experimentally measured transmittance without water condensation as shown in Figure S16b, Supporting Information. To suppress the oscillation of transmittance due to the nature of perfectly coherent wave optics, the total transmittance was calculated with 0.1 nm interval and the average taken over adjacent points over ± 25 nm. The water thickness of 16 µm was selected so that the predicted total transmittance best agreed with experimental measurements. The ray optics simulation was also conducted, giving the same results as the wave optics simulation (Figure S16b, Supporting Information).

To model the total transmittance through untreated LDPE film with water droplets, the ray optics simulation was done by using the commercial software COMSOL Multiphysics. The structure is shown in Figure S16a, Supporting Information. The same LDPE film thickness as that of treated LDPE film, and uniform radius of water droplets were assumed. The other geometrical parameters of the system were the diameter, contact angle, and areal density of water droplets. The diameter of the water droplets was set to be 80 µm, which approximately is the peak position of the radial distribution, and the contact angle of 110° was assumed. Those values were experimentally obtained as shown in Figure S6, Supporting Information. The areal density was treated as a fitting parameter and the best fit to experimentally measured total transmittance at 50 °C was produced when 0.55 was assumed.

Antifogging on Stretchable and Foldable Transparent Materials: To demonstrate the capability of eliminating fog on a stretchable transparent material, a Sylgard 184 was first thermally cured with a mixture ratio of 10:1 to fabricate a stretchable transparent material, and then the anti-fogging tape prestretched and the tape gently attached on the surface of the PDMS substrate. The surface of the PDMS substrate was exposed with the anti-fogging tape to heated water vapor (60 °C) to test its anti-fogging property. To demonstrate the capability of eliminating fog on a foldable transparent material, a PET film was first cut to a 2D shape that could be folded into a 3D cube, and thereafter our anti-fogging tape prestretched and the tape gently attached on the surface of the PET film. The 2D PET film was folded into a 3D cube with the anti-fogging tape as its inner surface. The inner surface of the 3D cube was exposed to heated water vapor (60 °C) to test its anti-fogging property.

Outdoor Water Purification Tests under Natural Sunlight: The solar water purification system was constructed from the super-absorbent foam (McMaster Carr, 8884k41) painted in black (Rust-Oleum Specialty), the pristine LDPE film or LDPE-PAAm film as the condenser, the glass beaker as the water collection tube, the bubble wrap as the thermal insulation layer, and the glass container as the basin filled with water of around 600 mL. A metallic ball was placed at the center of the condenser, driving the flow of the condensed water by its gravitational force. The outdoor water purification tests were conducted at Massachusetts Institute of Technology campus on June 23, 2020 and Sep 8, 2020. The solar flux, the ambient temperature, and the ambient relative humidity were recorded by the rooftop weather station at MIT Center for Advanced Urbanism. The temperatures of the absorber $T_{absorber}$, vapor (1 mm above the absorber) T_{vapor}, and the bulk water T_{water} were measured using thermocouples every hour. Collected purified water was measured using a balance with 0.001 g resolution. The ion concentrations of the collected water were measured using inductively coupled plasma mass spectrometry with calibrated results as shown in Figure S15, Supporting Information.

Supporting Information

Supporting Information is available from the Wiley Online Library or from the author.

Acknowledgements

S.L., X.Z., and G.C. acknowledge the funding support from the Abdul Latif Jameel Water and Food Systems Lab (J-WAFS) at the Massachusetts

Institute of Technology (MIT) under its seed grant program. The authors acknowledge the discussion with Dr. Xiaoyu Chen at MIT on the FTIR result and the discussion with Prof. Christoph Reinhart at MIT Center for Advanced Urbanism on the measurement of solar flux. The authors also acknowledge the Center for Environmental Health Sciences at MIT for supporting the usage of Inductively Coupled Plasma Mass Spectrometry, the support of which was provided by a core center grant P30-ES002109 from the National Institute of Environmental Health Sciences, National Institutes of Health. The authors thank A. F. Schwartzman in the NanoMechanical Technology Laboratory at MIT for help with AFM imaging. This work was supported by MIT.

Conflict of Interest

S.L., Y.Y., Y.T., X.Z., and G.C. have a provisional patent application number 63/197,294 on the design of a transparent and anti-fog polyethylene film.

Author Contributions

S.L., Y.Y., and J.N. contributed equally to this work. S.L. and G.C. conceived the idea. S.L. designed the study. S.L., Y.Y., J.N., X.L., and B.L. prepared the sample, conducted the UV–vis–NIR measurements, mechanical characterizations, FTIR measurements, HPLC measurements, outdoor solar tests, and anti-fogging eyeglass tests. Y.T. performed the simulations. S.L., Y.Y., J.N., X.L., Y.T., Y.T., J.Z., X.Z., and G.C. analyzed and interpreted the results. S.L. and G.C. wrote the manuscript with inputs from all authors.

Data Availability Statement

The data that support the findings of this study are available from the corresponding authors upon request.

Keywords

anti-fogging surfaces, hydrogel adhesion, personal protection equipment, solar water purification, transparent materials

Received: April 14, 2021
Revised: May 17, 2021
Published online:

[1] Y. Chen, Y. Zhang, L. Shi, J. Li, Y. Xin, T. Yang, Z. Guo, *Appl. Phys. Lett.* **2012**, *101*, 033701.
[2] I. R. Duran, G. Laroche, *Prog. Mater. Sci.* **2019**, *99*, 106.
[3] I. R. Durán, G. Laroche, *Adv. Colloid Interface Sci.* **2019**, *263*, 68.
[4] M. San-Juan, Ó. Martín, B. J. Mirones, P. De Tiedra, *Appl. Therm. Eng.* **2016**, *104*, 479.
[5] G. Ni, S. H. Zandavi, S. M. Javid, S. V. Boriskina, T. A. Cooper, G. Chen, *Energy Environ. Sci.* **2018**, *11*, 1510.
[6] Y. Xu, D. Kraemer, B. Song, Z. Jiang, J. Zhou, J. Loomis, J. Wang, M. Li, H. Ghasemi, X. Huang, *Nat. Commun.* **2019**, *10*, 1.
[7] C. Lamnatou, D. Chemisana, *Renewable Sustainable Energy Rev.* **2013**, *27*, 175.
[8] W. Yao, T. Wang, B. Jiang, F. Gao, L. Wang, H. Zheng, W. Xiao, S. Yao, W. Mei, X. Chen, *Br. J. Anaesth.* **2020**, *125*, e28.
[9] S. Ren, L. Wang, H. Yu, M. Haroon, R. S. Ullah, F. Haq, R. U. Khan, S. Fahad, *J. Coat. Technol. Res.* **2018**, *15*, 445.
[10] H. Lee, M. L. Alcaraz, M. F. Rubner, R. E. Cohen, *ACS Nano* **2013**, *7*, 2172.
[11] H. Dong, P. Ye, M. Zhong, J. Pietrasik, R. Drumright, K. Matyjaszewski, *Langmuir* **2010**, *26*, 15567.
[12] Z. Sun, T. Liao, K. Liu, L. Jiang, J. H. Kim, S. X. Dou, *Small* **2014**, *10*, 3001.
[13] M. Liu, S. Wang, L. Jiang, *Nat. Rev. Mater.* **2017**, *2*, 17036.
[14] X. Gao, X. Yan, X. Yao, L. Xu, K. Zhang, J. Zhang, B. Yang, L. Jiang, *Adv. Mat.* **2007**, *19*, 2213.
[15] Z. Han, X. Feng, Z. Guo, S. Niu, L. Ren, *Adv. Mater.* **2018**, *30*, 1704652.
[16] N. Nuraje, R. Asmatulu, R. E. Cohen, M. F. Rubner, *Langmuir* **2011**, *27*, 782.
[17] O. Tretinnikov, V. Pilipenko, L. Prikhodchenko, *Polym. Sci. Ser. B* **2012**, *54*, 427.
[18] Y. Yu, H. Yuk, G. A. Parada, Y. Wu, X. Liu, C. S. Nabzdyk, K. Youcef-Toumi, J. Zang, X. Zhao, *Adv. Mat.* **2019**, *31*, 1807101.
[19] M. F. Ashby, D. Cebon, *J. Phys. IV* **1993**, *3*, C7.
[20] N. Miljkovic, R. Enright, E. N. Wang, *ACS Nano* **2012**, *6*, 1776.
[21] Z. Huang, H. Ghasemi, *Adv. Colloid Interface Sci.* **2020**, 102264.
[22] J. Oh, R. Zhang, P. P. Shetty, J. A. Krogstad, P. V. Braun, N. Miljkovic, *Adv. Funct. Mater.* **2018**, *28*, 1707000.
[23] Z. Wu, N. Bouklas, R. Huang, *Int. J. Solids Struct.* **2013**, *50*, 578.
[24] F. Edition, *WHO Chron.* **2011**, *38*, 104.
[25] F. Zhao, Y. Guo, X. Zhou, W. Shi, G. Yu, *Nat. Rev. Mater.* **2020**, *5*, 388.
[26] L. M. Lozano, S. Hong, Y. Huang, H. Zandavi, Y. A. El Aoud, Y. Tsurimaki, J. Zhou, Y. Xu, R. M. Osgood, G. Chen, *Opt. Mater. Express* **2019**, *9*, 1990.
[27] Y. Xu, X. Wang, J. Zhou, B. Song, Z. Jiang, E. M. Lee, S. Huberman, K. K. Gleason, G. Chen, *Sci. Adv.* **2018**, *4*, eaar3031.
[28] S. Lin, X. Liu, J. Liu, H. Yuk, H.-C. Loh, G. A. Parada, C. Settens, J. Song, A. Masic, G. H. McKinley, *Sci. Adv.* **2019**, *5*, eaau8528.
[29] S. Lin, J. Liu, X. Liu, X. Zhao, *Proc. Natl. Acad. Sci. U. S. A.* **2019**, *116*, 10244.
[30] D. J. Segelstein, U. o. M.–K. City, **1981**.
[31] T. M. Nilsson, G. A. Niklasson, C. G. Granqvist, *Sol. Energy Mater. Sol. Cells* **1992**, *28*, 175.
[32] E. D. Palik, *Handbook of Optical Constants of Solids*, vol. *3*, Academic Press, San Diego, CA **1998**.